Cranial Perforation Using an Optically-Enhanced Surgical Drill

Konstantin Grygoryev , Katarzyna Komolibus, Jacqueline Gunther , Gerard Nunan, Kevin Manley, Stefan Andersson-Engels, and Ray Burke

Abstract—The design of mechanically clutched cranial perforators, used in craniotomy procedures, limits their performance under certain clinical conditions and can, in some cases, impose the risk of severe brain injury on patients undergoing the procedure. An additional safety mechanism could help in mitigating these risks. In this work, we examine the use of diffuse reflectance spectroscopy as a potential fallback mechanism for near real-time detection of the bone-brain boundary. Monte Carlo simulation of a two layer model with optical properties of bone and brain at 530 and 850 nm resulted in a detectable change in diffuse reflectance signal when approaching the boundary. The simulated results were used to guide the development of an experimental drill control system, which was tested on 10 sheep craniums and yielded 88.1% success rate in the detection of the approaching bone-brain boundary.

Index Terms—Diffuse reflectance spectroscopy, surgical guidance, cranial perforator, tissue boundary detection.

I. INTRODUCTION

CRANIOTOMY is a neuro-surgical procedure used to temporarily remove a section of the cranium, called the bone flap, in order to provide access to the brain for clinical assessment or treatment of brain lesions, traumatic brain injury or epilepsy[1], [2]. This procedure involves drilling a number of holes in the skull using a specialized drill. The burr, termed the cranial perforator (CP) and described for the first time in 1950 [3], was designed to reduce the risk of plunging into the cranial cavity during neurosurgery and causing injury or death. This instrument is a clever, mechanically clutched cutting tool which prevents the surgeon from boring into the dura or the brain by automatically disconnecting the CP from the drill motor once the inner surface of the cranium is breached. Despite the 70 years of tool refinement, relatively recent hospital investigations have shown that modern, clutched perforators can still fail to stop

under certain clinical conditions [4]–[7]. For the mechanical decoupling to be successful, the inner surface of the cranium must be perpendicular to the drilling axis, making this tool inadvisable for use in scenarios where the cranium is uneven or fractured. In addition, tool geometry, clutch mechanism design, the choice of the drilling site and the experience level of the surgeon have been noted to play a major role in plunging [8], [9]. To date, attempts to reduce the rate of plunging can be separated into two categories. The first category involves working around the shortcomings of the CP by modifying the surgical protocol to limit its use in scenarios where the risk of plunging is higher [4]. The second category employs advancements in the imaging, tracking and robotic technologies to improve the precision and outcome of neurosurgical procedures. Intraoperative tracking systems including magnetic tracking, optical tracking and real-time image acquisition can be used to superimpose the 3D position and orientation of surgical tools on the pre-operative CT, MRI or ultrasound images [10], [11]. These techniques, while proven successful, employ bulky, expensive equipment as well as influencing the operation procedure flow. In addition to tracking, a number of studies have used ultrasound to perform a direct bone thickness measurement with a tolerance of 1.2mm on *in vitro* samples [12], [13].

Diffuse reflectance spectroscopy (DRS) is a powerful tool used in the study of wavelength-dependent absorption and scattering properties of biological tissues. DRS has proved very useful in quantifying important information related to physiological properties of the tissue such as chromophore concentration or microstructure and has thus helped in the identification of tissue type [14], [15]. Recently, it has also been demonstrated that DRS can be used for controlling the drilling depth in orthopedic procedures [16]. In this biophotonics approach, differences in the optical properties of bone and blood-filled muscle were utilized to detect the boundary between the two tissue types in real time, while drilling through the bone. The boundary detection was achieved by comparing the intensity of diffusely reflected signals at 470 nm and 780 nm and relied on increased absorption of 470 nm relative to 780 nm as the thickness of the bone was reduced. The underlying concept behind this study relies heavily on the difference in blood content between the bone and the surrounding muscle, which served as a natural contrast agent. In combination with X-ray image guidance, broadband DRS has also been used to detect breaches of cortical bone in the human cadaver vertebrae during spinal screw placement [17], [18]. These studies have shown that an optically-enhanced pedicle

probe was capable of distinguishing between cancelous and cortical bone types on the basis of fat and blood concentration in the tissue. However, the application of DRS to dynamic boundary detection between cranial bone, dura matter or cerebral cortex, has not yet been demonstrated.

In this work, the feasibility of employing a two-wavelength DRS in craniotomy applications is examined. It is envisioned that such optical system could be integrated into a cranial perforator that retains the mechanical clutch systems as an additional method for boundary detection. In order to test whether cranial bone and brain can be optically differentiated, a Monte-Carlo (MC) simulation was performed to assess the effect of changing optical properties on the DRS signal. Guided by the results of the MC simulation, DRS modality was integrated into a custom CP drill bit and tested in craniotomy procedures on *ex vivo* sheep models in a controlled environment. Based on the MC simulation and the experimental findings of this study, we have shown that the bone-brain boundary can be successfully detected and thus DRS could be used in a smart clinical instrument for surgical guidance.

II. METHODS

A. Monte-Carlo Simulation

A simplified two layer MC simulations were performed using parallel computing, GPU based code called CUDAMCML [19], [20], based on a previously developed MCML code [21]. The meninges overlying the brain has been excluded from the model as these structures do not significantly affect light penetration into the brain[22]. Hence, two layer models are normally sufficient to accurately model the light propagation in the brain. The purpose for MC simulations was to examine the behaviour of 530 nm and 850 nm wavelengths as the bone thickness was decreased in order to predict the boundary position. The wavelengths have been selected in order to provide optical contrast between the brain and bone tissue. The 530 nm wavelength targets high hemoglobin absorption in the brain, while 850 nm wavelength provides reference signal and deeper penetration depth. Simulations were run with bone thicknesses ranging from 6mm to 0 mm in steps of 0.25 mm to mimic drilling through cranium. The MC model consisted of one source and one detector fiber 600 μm in diameter coupling light in and out of a two layer model of scattering media (bone and brain). The source beam was convolved with a guassian profile using techniques from [23]. The input powers were weighted according to the LEDs in the probe (6.8 mW for 530 nm and 10.5 mW for 850 nm). The output reflectance was integrated over the detector area. The distance between source and detector was set to 1.3mm. The optical properties used in the simulation were previously described in [24], [25] and are listed here in Table I. In the simulations, the anisotropy factor was set to $g = 0.9$ and 1×10^6 photon packages were injected from the source fiber.

B. Samples

The CP experiments were performed on $n = 10$ sheep heads sourced from a local butcher. The sheep were slaughtered on the

	Brain			Bone		
	μ_a	μ'_s	n	μ_a	μ'_s	n
530 nm	2.5	6	1.41	0.5	13	1.55
850 nm	0.12	4	1.39	0.08	10	1.55

day preceding the measurements. The skin was removed immediately and heads were then kept in a fridge at 4°C overnight prior to the commencement of the experiment. During the measurements the heads were secured in a head clamp (Mayfield, USA). A number of different locations on the skull, ranging from 4 to 14 per head, were chosen for drilling to allow for the CP performance to be tested for varying bone thicknesses. Any thick connective tissue or muscle overlying the drilling location were cut away using a scalpel prior to drilling. Prior to the commencement of the experiment, an initial opening in the skull was made to ensure that measurements would began in pure cortical bone. The forward drilling was accomplished by manually applying axial pressure to the drill. Maximum possible RPM of the drill was used during each measurement. This was achieved by simply pressing the trigger fully. The experiments were performed by researchers not having prior experience in a surgical setting and hence the forward drilling was not influenced by any tactile or auditory feedback which an experience surgeon would use to prevent plunging.

C. DRS-Drill Integration

In a similar manner to that previously described in [16], the DRS sensing was integrated into a modified version of a commercial surgical drill (CD4, Stryker, USA) presented in Fig. 1a. The most critical modifications of the drill involved the integration of 18 photodiodes (PDs) into the drill's chuck and optical fibers inside the CP burr. The PDs (S-4V, OSI Optoelectronics, USA) were mounted onto a flex-PCB, with output signals electrically connected in parallel with one another and operated in photovoltaic mode. The flexible, conductive substrate allowed the PD array to be formed into a barrel and in order to maintain the shape, the array was glued into a custom, 3D printed cartridge. The whole assembly was then installed into the drill's chuck where each PD faced the rotational axis of the CP. This arrangement allowed the array to measure the intensity of collected light through the entire 360° CP rotation.

To deliver and collect light to and from the surface of the bone, a custom CP burr was machined and integrated with two silica optical fibers (600 μm core diameter, NA 0.51, ThorLabs, UK). Both fibers terminated on the same relief surface of the CP, 1.3mm apart to match the MC simulation Fig. 1b). The illumination scheme included two LEDs, 530 nm and 850 nm (M530F2, M850F2, ThorLabs, UK), guided by a custom-made bifurcated Y-bundle which consisted of two 400 μm (NA 0.51, ThorLabs, UK) silica fibers, coupled to the LEDs via SMA905
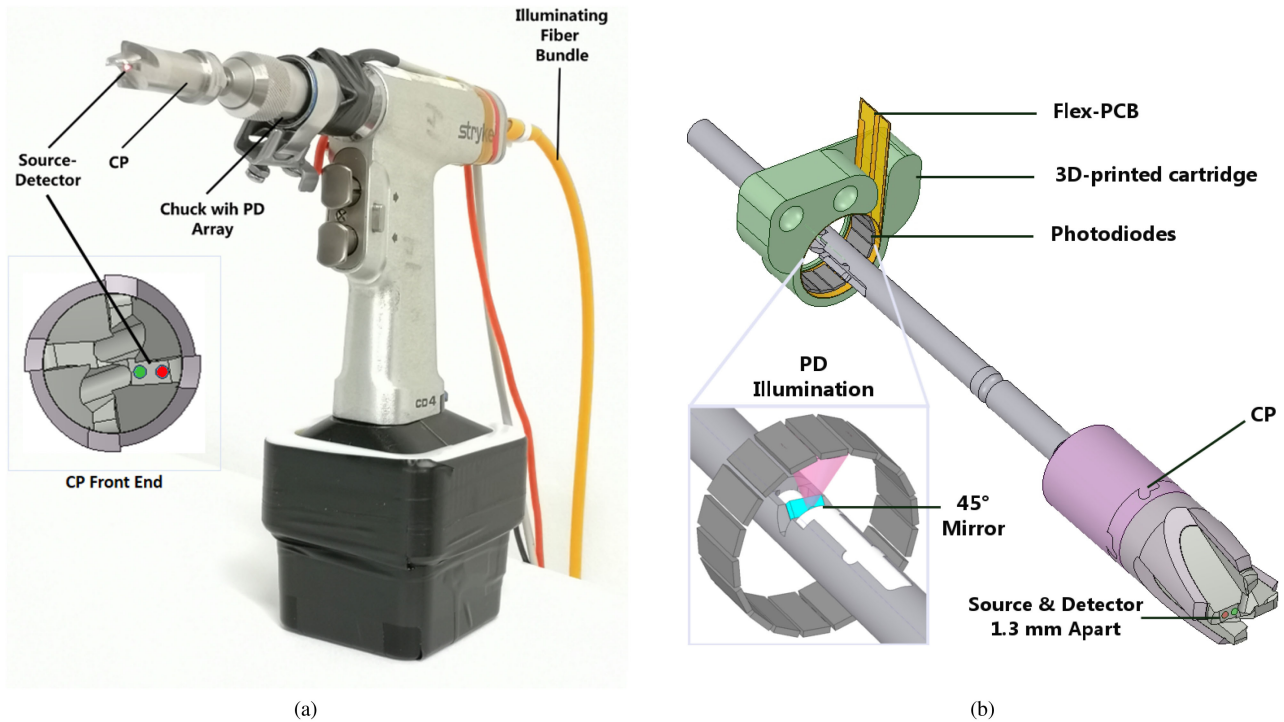
Fig. 1. Surgical drill with integrated DRS sensing modality. (a) Commercial surgical drill used in this study. The inset shows the relative location of source (green) and detector (red) optical fibers to CP cutting geometry. (b) An image illustrating the custom-designed CP with dedicated detection system. The source and detector fibers are running along a machined channel inside of the shaft and the CP body, terminated at the tip of the drill bit with two separate openings with 1.3 mm inter-fiber distance. The detector fiber delivers the light to the PD array, which is mounted inside a 3D-printed cartridge using the Flex-PCB. The inset shows the method of PD illumination. The light collected by the detector fiber is patched to the 45° mirror, mounted inside the CP shaft. In turn, the mirror reflects the light onto the PD array as the CP rotates.

connectors. At the other end, the fiber bundle was merged into a single 1 mm (NA 0.51, ThorLabs. UK) silica fiber, sealed inside a cylindrical holder and terminated with a 2 mm sapphire ball lens (Swiss Jewel Company, USA) using UV adhesive (Norland 68, Norland, USA). The cylindrical holder was designed to fit into the cannula port at the back of the surgical hand drill and allowed secure attachment of the illuminating fiber bundle to the drill body. The light from the illumination bundle was subsequently coupled to the source fiber of the CP via a second sapphire ball lens. The CP's collection fiber was terminated at a mirror, positioned within the CP shaft at 45° relative to the longitudinal axis. High reflection efficiency was achieved by using high-performance specular reflector film with nominal reflectance greater than 98.5% within wavelength range used in this study (ESR, 3M, USA). Once the CP was installed in the drill, the position of the mirror was adjusted in order to align it with the PD array located within the drill chuck.

D. Data Acquisition

The full schematic of the experimental setup including light delivery, collection and data acquisition is presented in Fig. 2. During the experiment, user-developed LabView software was used to manage the data acquisition device (DAQ, USB-6003, National Instruments, USA). In order to perform the two-wavelength DRS measurements, the 530nm and 850nm LEDs were pulsed 180° out of phase at 400Hz and 50% duty cycle via

the analog output channel of the DAQ. The duration of a full LED cycle was therefore 2.5 ms. The integrated signal from the PD array produced an electrical current proportional to the intensity of the diffuse light. The current signal was converted to analog voltage and amplified using a one channel trans-impedance amplifier (TIA, SR570, Stanford Research Systems). To reject high frequency noise and integrate the signal over an appropriate time period, a low pass filter (3 kHz, 12 dB) was applied. The filtered, amplified signal was then sampled at 20kHz. The data acquisition and LED pulses were hardware synchronized and triggered from the computer by a TTL pulse fed to the PIO and PIF inputs of the DAQ. Using this method of synchronization, the collected data points were referenced with 1.25ms pulses of the 530 nm and 850 nm LEDs. For a given modulation and sampling frequency (400 Hz, 20 kHz, respectively) each full measurement cycle corresponded to 50 data points. With a 50% duty cycle this equates to 25 measurements while each LED is on.

E. Boundary Detection and Triggering Condition

The signal processing flowchart is presented in the Fig. 3. The data processing scheme can be divided into three building blocks: (1) initialisation, (2) drilling in the bone and (3) boundary detection. During the initialisation phase, the raw experimental data is collected at a sampling rate of 20 kHz (Fig. 3a). This allows for the determination of the average response of the
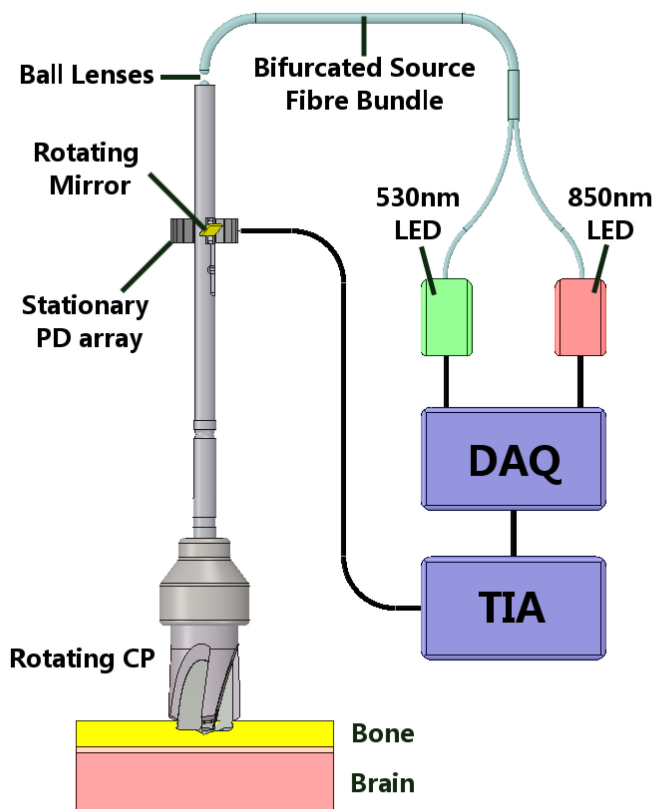
Fig. 2. Schematic of integrated CP system showing the key components used for LED control and data acquisition. Computer-controlled DAQ module was used to trigger the LEDs. The intensity of diffusely reflected light was collected by the PD array, filtered and amplified using TIA and then sampled by DAQ.

system in pure cortical bone for normalisation purposes. To account for the switching times of the LEDs and the low pass filter, only the middle 15 points of the 25 measurement points per LED are used for calculating the average voltage signal at each given illumination wavelength. These averaged data points, corresponding to each LED, are acquired for 200 ms (corresponding to 80 full measurement cycles) and subsequently subtracted from one another to calculate an initial averaged differential signal (Fig. 3b). The differential voltage value then is used to normalise the data while drilling in the bone (Fig. 3c). In order to further reduce measurement noise arising from the movement of opto-mechanical parts, a running average over 300 ms corresponding to 120 measurement cycles is applied to the differential signal (Fig. 3d). The approaching bone-brain boundary can be detected via two different algorithms which can be run simultaneously: threshold and slope. The condition values for both detection schemes were found empirically by drilling through three additional sheep heads (not taken into account in the final results of this study) and monitoring the diffuse reflectance signal while intentionally plunging. The threshold scheme relies on monitoring the normalised level of the differential signal over the period of 100ms and was found to be 75% of the nominal signal. When the signal drops below this threshold value, the software records this event as a boundary

detection and triggers the drill to stop as shown in Fig. 3e. The slope scheme relies on changes in the gradient of the normalised differential signal. It involves performing a linear fit over a period of 200ms with the slope trigger condition set to −0.8. When the slope of the signal reaches −0.8, the software records the event as boundary detection and triggers the drill to stop as shown in Fig. 3f. The two algorithms probe the differential signal in parallel, while the software sends an electrical signal via the DAQ to a relay, mounted inside the drill battery, which stops the motor of the drill when either of the two conditions is first met

III. RESULTS

A. Monte-Carlo Simulations

As a result of MC simulation in the two layer model (bone and brain) for different thicknesses of the bone layer, a photon hitting density map was created (Fig. 4). Based on these color maps the intensity of both wavelengths collected by the detector fiber at a distance of 1.3 mm from the source were extracted and showed as a function of the bone layer thickness in Fig. 5a). The reflectance of 530 nm remained constant in the bone layer for thicknesses larger than 2 mm and was then observed to decrease until the layer thickness was reduced to 0mm. The behaviour of 850 nm was different and was observed to decrease slowly until the bone layer thickness was approximately 2 mm. Below 2 mm, the reflectance decreased at a higher rate. The unique behaviour of both wavelengths is highlighted by the difference plot and suggests that, theoretically, the boundary starts influencing the DRS measurement when the bone layer is less than 4mm thick. Interestingly, the ratio plots are less sensitive to the approaching boundary and only highlight an approaching boundary at bone thicknesses below 1 mm.

B. DRS-Assisted Drilling

Fig. 5b presents an example of experimental diffuse reflectance intensity data for 530 nm (green) and 850 nm (red) wavelengths when drilling through cranial bone. In addition, difference and ratio plots for the two wavelengths are shown for comparison. The experimental data mimics the situation considered in the MC simulation, except for well defined thickness of cranial bone. As the rate of drilling was also unknown, the data was thus plotted with respect to time, rather than distance as shown in the simulation plot. As described above, the triggering conditions for both slope and threshold have been set to -0.8 and 75%, respectively. The graphs indicate that the magnitude of diffuse reflectance for both wavelengths remains relatively constant for the period of 0–6s. During this time, the CP was cutting through the bulk of the cranial bone. Between 6s and 8.5 s, the magnitude of 850 nm signal was observed to decrease at a higher rate relative to 530 nm. The distinct behaviour of 850 nm is also highlighted by the differential curve and, to a lesser extent, by the ratio graph. The decreasing reflectance intensities indicate that the CP was approaching the boundary between the cranium and the brain. A sharp drop in intensity of the difference between 850 nm and 530 nm was observed at 8.5s suggesting that the CP is either close to the bone-brain boundary or has
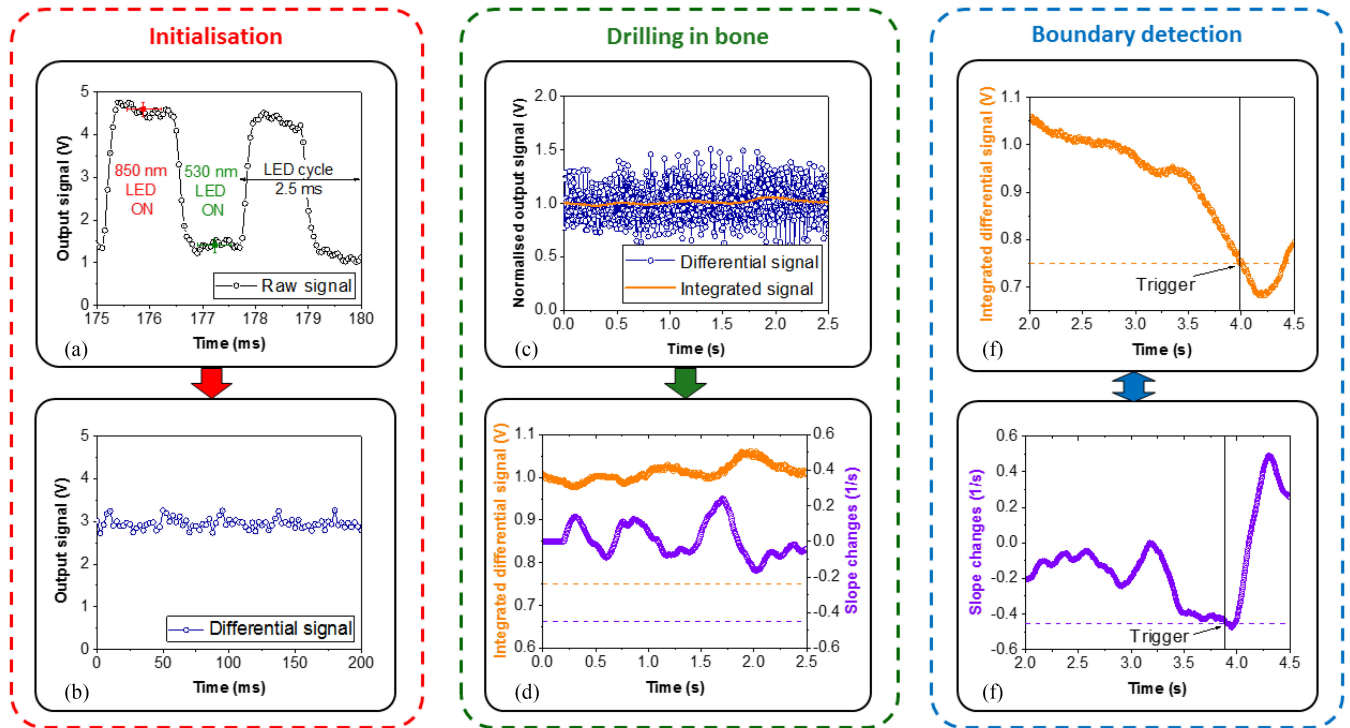
Fig. 3.   Flow chart describing the signal processing used to detect bone-brain boundary in near real-time: a) Example of a raw signal of two LED cycles at 400 Hz, sampled at 20 kHz, b) Signal calculated as difference between averaged intensity at 850 nm and 530 nm of each LED cycle, c) Differential signal normalized to 1 and integrated over 300 ms, d) Monitoring threshold and slope condition simultaneously in real time, e) Threshold condition reached, trigger signal sent to the drill, f) Slope condition reached, trigger sent to the drill.
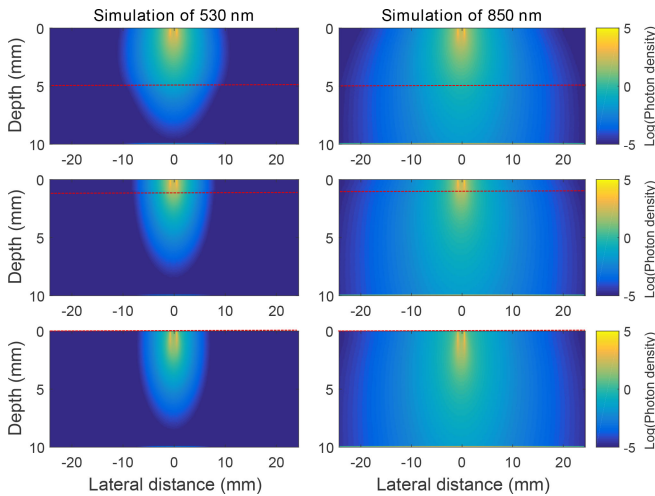

Fig. 4.   MC simulated photon hitting density map for 530nm (left) and 850nm (right) wavelengths as well as bone thickness of 5mm (top), 1mm (middle) and 0mm (bottom). The red dashed lines indicate the position of bone-brain boundary.

broken through the boundary and stopped without plunging. The approaching boundary was detected by the threshold algorithm at 8.4s when the intensity of the differential signal decreased below 75% of its normalized value. The trigger signal was sent to the drill, which was successfully stopped just before reaching the bone-brain boundary. The decrease in the signal following the trigger timestamp is related to the fact that even after stopping

the drill, the data acquisition continues and undergoes processing of 300 ms moving average. After that the signal reaches stable level when the drill has stopped and data acquisition is manually terminated. Overall, the experimentally obtained data presented in this figure agree with the simulation and show that the DRS can be used to detect the bone-brain interface prior to the breach.

In total, the DRS-enhanced CP was used to perform $n = 84$ measurements in 10 sheep craniums on both sides of saggital sutures. The duration of the drilling ranged between 5 and 40s and was influenced by the thickness of the skull at the drilling site in addition to the speed of the drill. The outcomes of the experiments were split into five categories, listed in Table II.

The "Perfect Stop" (51.2%) outcome was observed when the CP stopped just prior to plunging, leaving a thin, less than 1mm thick, bone membrane as shown in Fig. 6a (i) and (ii). In this figure, the holes were illuminated from behind using a 850nm LED to highlight the thinnest parts of the bone shelf with intense blue hue. The black areas display the areas where the bone shelf was pierced with a scalpel to examine its remaining thickness. In all examples of Perfect Stop, the dura remained intact (result not shown). The "Color Change" (19%) outcome was observed when CP stopped automatically in response to bone pigmentation as shown in Fig. 6b (iii). In such cases, the thickness of remaining bone was still exceeding 1mm and the measurement was continued afterwards. The "Plunge Stop" (17.8%) was observed when the CP stopped after it plunged through the bone-brain boundary, damaging the dura and the brain tissue. The "Perfect Stop", "Color Change" and "Plunge Stop" outcomes comprised 88.1% of all experiments and were
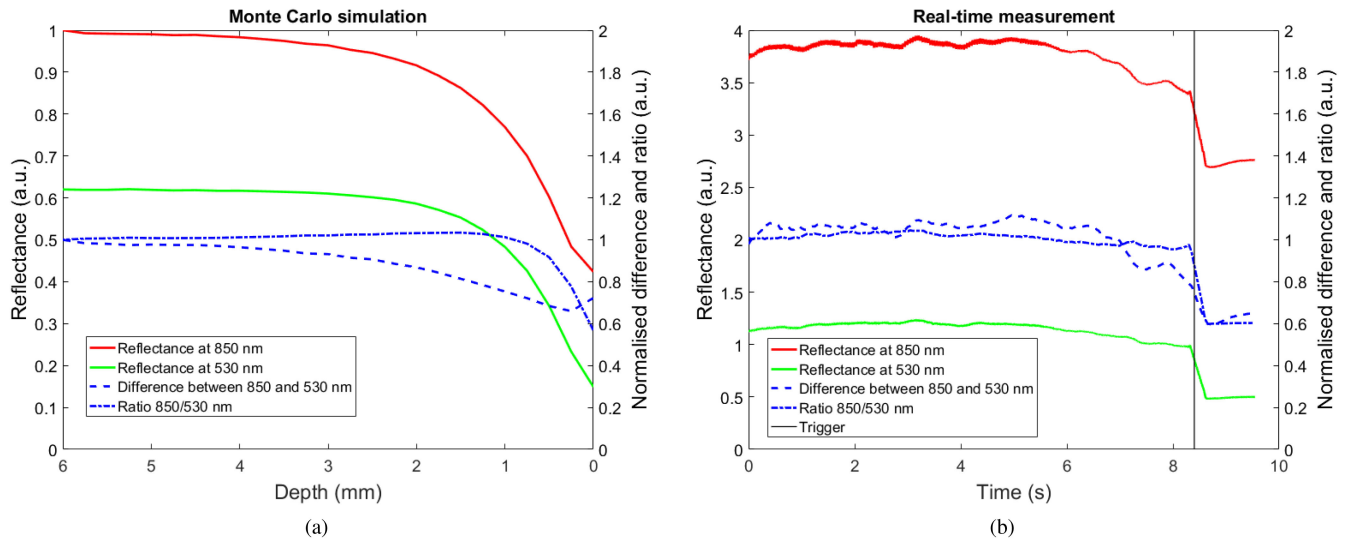
Fig. 5. a) MC simulation showing the behaviour of 530nm and 850nm wavelengths in a layer of bone at a distance of 0-6mm from bone-brain interface. b) Experimental measurements showing the response at 850nm and 530nm wavelengths to the approaching bone-brain interface. Both figures also show the difference and ratio plots (in blue) which highlight the effects of changing optical properties on each wavelengths.

TABLE II
RESULTS SUMMARY

Exp No.	Heads	Measurements	Perfect Stop	Color Change	Plunge Stop	False Positive	Plunge
1	2	16	10	0	4	0	2
2	2	12	10	0	2	0	0
3	2	27	10	11	2	3	1
4	2	21	10	5	2	4	0
5	2	8	3	0	5	0	0
Total	10	84	43	16	15	7	3
Percentage		100	51.2	19	17.9	8.3	3.6

considered as positive results. While a "Plunge Stop" result would not be acceptable in a clinical setting, for the purpose of the optical experiments it was deemed successful as the system did respond to a change in optical properties once the CP had broken through the cranial bone. The delayed response in this case could be related to data integration period during processing or reaction of the battery relay, both of which could be improved in the future experiments.

The "False Positive" (FP, 8.3%) and "Plunge" (3.6%) made up the remaining 11.9% of experiments. These tests were considered as negative outcomes. In the case of FP, the CP automatically stopped in bone of uniform color, as shown in Fig. 6b (iv), indicating that the stop was not triggered by a change in optical properties. Lastly, in the experiments classified as plunge, the CP did not detect the approaching boundary, plunged and continued rotating until the button on the drill was released.

IV. DISCUSSION

A. Diffuse Reflectance

This study illustrates the potential of integrating DRS-based optical guidance into a surgical tool. More specifically, this first attempt employed two wavelengths, 530 nm and 850 nm, to detect the boundary between cranial bone and the underlying brain by dynamically measuring the changes in diffuse reflectance as suggested by the previous, related study [16]. To date, there has been a limited number of studies investigating optical integration into surgical tools for direct measurements and surgical guidance [17], [18], [26]. Instead, a large number of investigations have concentrated on indirectly controlling the surgical instruments by using complicated motion tracking systems in combination with potentially harmful, pre-operative imaging [10], [27]. The implementation of motion tracking in the operating theater significantly increases cost because it requires additional equipment such as multiple cameras as well as computers for real time image processing. In addition, camera based systems are susceptible to line-of-sight occlusions by medical staff while the pre-operative images may not accurately represent the biological structures due to anatomical changes that may occur prior to surgery. Both of these factors reduce the accuracy of motion tracking-based surgical guidance systems. In this respect, an optical system with direct measurement capability is advantageous because it does not require additional referencing information and potentially can be miniaturized for easier integration into
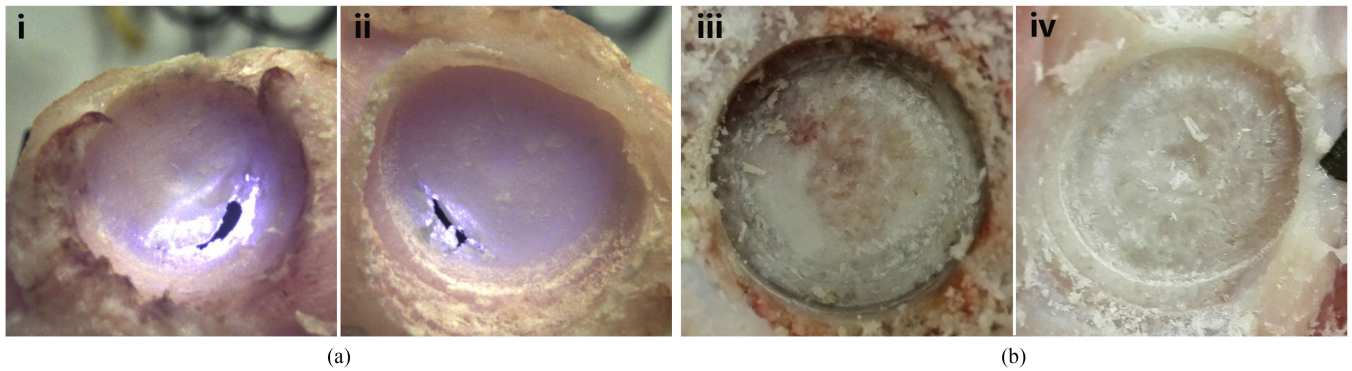
Fig. 6. a) (i) and (ii) Images of remaining bone shelf after CP detected the approaching bone-brain boundary and stopped automatically. both drilling sites were illuminated with 850nm LED (blue hue) from the back to highlight the variation of the bone shelf thickness. The intense white and blue areas indicate the thinnest parts of the shelf while the black areas indicate where the bone shelf was pierced with a scalpel to probe its thickness. b) (iii) A thick bone shelf showing dark red areas caused by the presence of blood vessels that triggered the CP to stop. (iv) A thick bone shelf without any obvious color defects presenting the FP case where the CP stopped automatically.

existing surgical tools. The direct optical sensing of cranial perforator has the potential to allow the surgeons to perform craniotomy on areas of the skull that are fractured or have uneven thickness. Furthermore, DRS in combination with the existing clutched mechanisms could further mitigate the risks of brain damage or death associated with cranial perforator plunge.

This study successfully demonstrated that the dynamic DRS measurements can be used to control the depth of the CP and prevent the plunge. Specifically, the tests performed on sheep heads have shown that the difference between bone and brain optical properties can be used to prevent the CP from plunging and damaging the dura during a craniotomy procedure. Furthermore, in a number of experiments the CP was able to detect blood vessels as well as pigmentation of the cranial bone. To improve further the discrimination between bone and brain layers as well as avoiding the detection of blood vessels in the cortical bone, additional contrast agents present in different spectral regions, such as water and lipid, could be used. Implementation of infrared light sources (in the 1200nm-2000nm region) and employment of suitable detectors have the potential to take advantage of these absorption peaks [28].

B. Mechanics and Packaging

In this study, a number of difficult mechanical challenges associated with coupling light from stationary LEDs into a rotating assembly and back into stationary detectors were addressed. First, utilizing silica optical fibers ensured that the light transmission in and out of the CP did not degrade with every consecutive test. It was possible to use the same cutting head to perform multiple tests. This was a critical achievement as assembly of a single CP took a considerable amount of time and effort. It is important to note that the 600 μm silica optical fibers have a relatively large bending radius and thus in order to package them inside the CP, the cutting geometry had to be modified. As a consequence, the new cutting geometry was noted to be less efficient in terms of chip clearing and led to packing

of the flutes when drilling through particularly thick portion of the cranium. In such cases, the CP had to be retracted out of the cranium to clean the flutes and the packed bone material had to be removed. It was also attempted to maintain the original cutting geometry and instead reduce the fiber size to 400 μm to allow for more fiber flexibility. Unfortunately, the smaller diameter fiber delivered and collected very little light, resulting in very low detectability. This technical issue can be compensated for in the future by more powerful and coupled with higher efficiency light sources.

Second, as compared to previous versions, the detection of diffuse light was improved by using a custom 3D printed cassette as the foundation for the PDs. The cassette insured that the Flex-PCB maintained a barrel shape, preventing it from collapsing into the center. The collapse of the Flex-PCB has been previously noticed in the preceding prototype and its effect was the cyclic modulation of PD array output caused by unequal distances between the PDs and the mirror. Furthermore, the cassette ensured that the entire PD array was better aligned with the mirror.

Third, the effects of opto-mechanical misalignment were addressed by using two-wavelength illumination where both wavelengths recorded the same cyclic signal fluctuations, which were then removed as discussed in the following section. The challenge of optical misalignment primarily stemmed from the fact that the setup used in this research was not designed for cranial perforation nor optical integration. Rather, the particular hardware was identified as a suitable donor platform for DRS integration and demonstration of the technology. Although, the drill and the chuck have been engineered and manufactured to the tightest mechanical tolerances, a certain level of flexibility must be incorporated into the coupling mechanisms to allow the chuck to be easily attached and detached from the drill. During this project, it was observed how this flexibility, while suitable for mechanical coupling, causes challenges with optical alignment and mechanical noise. Future work could be focused on developing coupling mechanisms with enhanced optical alignment while maintaining coupling flexibility.

C. Data Processing

In addition to detection of bone-brain boundary, the use of two wavelength illumination also helped with reducing the effects of opto-mechanical misalignment and cyclic signal fluctuation. The LED modulation frequency of 400 Hz resulted in approximately 30 pulses per rotation of the CP for both light sources. At this rate, both LEDs pulsed once within 12° of CP rotation and experienced a similar level of attenuation due to optical misalignment. The intensity difference between each pair of illuminating pulses remained constant, making it possible to partially remove the cyclic noise by subtracting first intensity measurement from the following one. Additional integration of the subtracted signal reduced the misalignment noise further. Although effective, this data processing method impacted the response time of the drill to the approaching boundary. This lag may be the reason behind the plunging of the CP into the brain prior to the automated stop in 17.9% of tests. Hence, to improve response time of the drill, the opto-mechanical noise must be dealt with at the hardware level as discussed below.

D. Future Integration

The potential area where improvements to performance could be made is reducing the number of optical coupling stages as well as removing any mechanical movement between optical components. This may be achieved by integrating the illumination and detection capability into the cutting tool itself. Micro-LEDs may be a suitable for such integration due to their relatively small size and high irradiance power in range of 250 mW/mm^2 [29]. Coupling these types of devices to a short silica fiber using micro-optics would ensure minimal illumination losses [29], [30]. Similarly, a short collecting fiber could be coupled to a micro PD, positioned within the rotating CP. The integration of illumination and detection into the rotating CP in theory should enhance detectability, remove some of the challenges associated with coupling light from stationary assemblies into moving parts and most importantly, remove the mechanical noise associated with dynamic, optical misalignment. Although, it is important to acknowledge that integration of optics into the CP will result in a different set of challenges. Primarily, the electronic control of the LEDs and data collection from the PD during high speed rotation will need to be addressed.

Ultimately, the DRS capability will need to be integrated into the clutched CP to provide an additional mechanism that stops the perforator when drilling through uneven or compromised areas of the cranium. Such integration presents additional set of challenges in terms of packaging the optics and electronics due to the fact that most of the space inside the CP is occupied by the mechanical clutch mechanism.

V. Conclusion

This study has successfully showcased the potential of DRS-integrated cranial perforator. The drilling experiments performed on sheep craniums showed that the bone-brain boundary can be optically detected when drilling through the cranial bone. In addition, these tests strongly indicated that optical detection can be used to trigger the drill motor to stop automatically before the CP plunges into the cranial cavity. This study has also addressed a number of difficult opto-mechanical challenges and as a result produced a robust, optically-enhanced cutting tool capable of drilling multiple holes without any observable degradation.

References

[1] V. DiNapoli and Y. Gozal, "Craniotomy," 2018, Mayfield Certified Health Info, Mayfield Clinic, Cincinnati, Ohio. [Online]. Available: https://mayfieldclinic.com/pe-craniotomy.html

[2] W. Stummer, M. J. van den Bent, and M. Westphal, "Cytoreductive surgery of glioblastoma as the key to successful adjuvant therapies: New arguments in an old discussion," *Acta Neurochirurgica*, vol. 153, no. 6, pp. 1211–1218, 2011.

[3] G. W. Smith, "An automatic drill for craniotomy," *J. Neurosurgery*, vol. 7, no. 3, pp. 285–286, 1950.

[4] T. W. Vogel, B. J. Dlouhy, and M. A. Howard, "Don't take the plunge: Avoiding adverse events with cranial perforators," *J. Neurosurgery*, vol. 115, no. 3, pp. 570–575, 2011.

[5] J. Caird and K. Choudhari, "Plunging during burr hole craniostomy: A persistent problem amongst neurosurgeons in britain and ireland," *British J. Neurosurgery*, vol. 17, no. 6, pp. 509–512, 2003.

[6] M. Beniwal and D. Shukla, "Management of perforator plunge in the transverse sinus," *Pediatric Neurosurgery*, vol. 51, no. 5, pp. 273–275, 2016.

[7] M. Ito *et al.*, "Penetrating injury of the brain by the burr of a high-speed air drill during craniotomy: Case report," *J. Clin. Neurosci.*, vol. 8, no. 3, pp. 261–263, 2001.

[8] Y. Murai *et al.*, "Reuse of a reversed bone pad to perforate incompletely penetrated burr holes created by automatic-releasing cranial perforators," *Operative Neurosurgery*, vol. 13, no. 3, pp. 324–328, 2017.

[9] "Cranial perforators with an automatic clutch mechanism, failure to disengage," FDA, FDA Safety Communication, 2015.

[10] J. A. Smith *et al.*, "30 years of neurosurgical robots: Review and trends for manipulators and associated navigational systems," *Ann. Biomed. Eng.*, vol. 44, no. 4, pp. 836–846, 2016.

[11] C.-C. Lin *et al.*, "Neurosurgical robotic arm drilling navigation system," *Int. J. Med. Robot. Comput. Assisted Surgery*, vol. 13, no. 3, 2017, Art. no. e1790.

[12] A. Follmann *et al.*, "A novel concept for smart trepanation," *J. Craniofacial Surgery*, vol. 23, no. 1, pp. 309–314, 2012.

[13] S. H. Tretbar, P. K. Plinkert, and P. A. Federspil, "Accuracy of ultrasound measurements for skull bone thickness using coded signals," *IEEE Trans. Biomed. Eng.*, vol. 56, no. 3, pp. 733–740, Mar. 2009.

[14] T. M. Bydlon *et al.*, "Chromophore based analyses of steady-state diffuse reflectance spectroscopy: Current status and perspectives for clinical adoption," *J. Biophotonics*, vol. 8, no. 1-2, pp. 9–24, 2015.

[15] D. J. Evers *et al.*, "Diffuse reflectance spectroscopy: Towards clinical application in breast cancer," *Breast Cancer Res. Treatment*, vol. 137, no. 1, pp. 155–165, 2013.

[16] M. Duperron *et al.*, "Diffuse reflectance spectroscopy-enhanced drill for bone boundary detection," *Biomed. Opt. Express*, vol. 10, no. 2, pp. 961–977, 2019.

[17] A. Swamy *et al.*, "Diffuse reflectance spectroscopy, a potential optical sensing technology for the detection of cortical breaches during spinal screw placement," *J. Biomed. Opt.*, vol. 24, no. 1, 2019, Art. no. 017002.

[18] A. Swamy *et al.*, "Validation of diffuse reflectance spectroscopy with magnetic resonance imaging for accurate vertebral bone fat fraction quantification," *Biomed. Opt. Express*, vol. 10, no. 8, pp. 4316–4328, 2019.

[19] E. Alerstam, T. Svensson, and S. Andersson-Engels, "Parallel computing with graphics processing units for high-speed Monte Carlo simulation of photon migration," *J. Biomed. Opt.*, vol. 13, no. 6, 2008, Art. no. 060504.

[20] E. Alerstam *et al.*, "Next-generation acceleration and code optimization for light transport in turbid media using gpus," *Biomed. Opt. Express*, vol. 1, no. 2, pp. 658–675, 2010.

[21] L. Wang, S. L. Jacques, and L. Zheng, "MCML–Monte Carlo modeling of light transport in multi-layered tissues," *Comput. Methods Programs Biomedicine*, vol. 47, no. 2, pp. 131–146, 1995.

[22] S. J. Madsen and B. C. Wilson, "Optical properties of brain tissue," in *Optical Methods and Instrumentation in Brain Imaging and Therapy*. Berlin, Germany: Springer, 2013, pp. 1–22.

[23] L. Wang, S. L. Jacques, and l. Zheng, "Conv–convolution for responses to a finite diameter photon beam incident on multi–layered tissues," *Comput. Methods Programs Biomedicine*, vol. 54, no. 3, pp. 141–150, 1997.

[24] S. Gebhart, W. Lin, and A. Mahadevan-Jansen, "In vitro determination of normal and neoplastic human brain tissue optical properties using inverse adding-doubling," *Phys. Medicine Biol.*, vol. 51, no. 8, pp. 2011–2027, 2006.

[25] A. Farina *et al.*, "In-vivo multilaboratory investigation of the optical properties of the human head," *Biomed. Opt. Express*, vol. 6, no. 7, pp. 2609–2623, 2015.

[26] D. H. Wicaksono *et al.*, "Micro-optics assembly in dental drill as a platform for imaging and sensing during surgical drilling," in *Proc. SENSORS*, 2010, pp. 265–268.

[27] P. Bast *et al.*, "Robot-and computer-assisted craniotomy: Resection planning, implant modelling and robot safety," *Int. J. Med. Robot. Comput. Assisted Surgery*, vol. 2, no. 2, pp. 168–178, 2006.

[28] S. L. Jacques, "Optical properties of biological tissues: A review," *Phys. Medicine Biol.*, vol. 58, no. 11, pp. R37–R61, May 2013.

[29] N. Grossman *et al.*, "Multi-site optical excitation using ChR2 and micro-led array," *J. Neural Eng.*, vol. 7, no. 1, 2010, Art. no. 016004.

[30] L. Chaudet *et al.*, "Development of optics with micro-led arrays for improved opto-electronic neural stimulation," in *Optogenetics: Optical Methods for Cellular Control*, vol. 8586. International Society for Optics and Photonics, 2013, Art. no. 85860R.